

# Spectrally Tunable and Stable Electroluminescence Enabled by Rubidium Doping of CsPbBr<sub>3</sub> Nanocrystals

Petar Todorović, Dongxin Ma, Bin Chen, Rafael Quintero-Bermudez, Makhsud I. Saidaminov, Yitong Dong, Zheng-Hong Lu, and Edward H. Sargent\*

Perovskite nanocrystals exhibit high photoluminescence quantum yields (PLQYs) and tunable bandgaps from ultraviolet to infrared. However, blue perovskite light-emitting diodes (LEDs) suffer from color instability under applied bias. Developing narrow-bandwidth deep-blue emitters will maximize the color gamut of display technologies. Mixed anion approaches suffer from halide segregation that leads to their spectral instability. Here instead, a mixed cation strategy is employed whereby Rb<sup>+</sup> is directly incorporated during synthesis into CsPbBr<sub>3</sub> nanocrystals. Blue-emitting perovskite quantum dots (QDs) with stable photoluminescence, PLQYs greater than 60%, tunable emission from 460 to 500 nm, and narrow emission linewidths (<25 nm) are reported. The strategy retains a pure bromine crystal structure resulting in color-pure stable electroluminescence at operating voltages of up to 10 V, peak external quantum efficiencies (EQEs) of 0.87% and 0.11% for sky-blue (490 nm), and deep-blue (464 nm) devices. The sky-blue devices exhibit the highest combined luminance of 93 cd m<sup>-2</sup> at an EQE of 0.75%, the best reported to date of perovskite QD LEDs.

In the past decade, perovskites have emerged as a novel class of semiconductor materials for light emission and light harvesting.<sup>[1–6]</sup> Lead-halide perovskites take the form APbX<sub>3</sub>, where A is a monovalent cation [i.e., Cs<sup>+</sup>, CH<sub>3</sub>NH<sub>3</sub><sup>+</sup> (methylammonium, MA<sup>+</sup>), CH(NH<sub>2</sub>)<sub>2</sub><sup>+</sup> (formamidinium, FA<sup>+</sup>)], and X is the halogen anion (i.e., Cl<sup>-</sup>, Br<sup>-</sup> or I<sup>-</sup>). These perovskites exhibit efficient charge transport, tunable bandgaps, high absorption coefficients, and narrow emission linewidths.<sup>[3,7–9]</sup> These materials are solution-processable as bulk (3D), quasi-2D, 2D, and colloidal nanocrystal (0D) materials, each showing promise in enhancing optoelectronic devices.

Perovskite quantum dots (QDs) have been employed in light-emitting applications in light of their high photoluminescence

quantum yields (PLQYs), as well as their tunability through size and composition which enables emission wavelengths that span the full visible spectrum.<sup>[1,10–12]</sup> In contrast with conventional epitaxially grown semiconductors, solution-processed quantum dots are synthesized at lower temperatures, which enables low-cost device fabrication and compatibility with flexible plastic substrates. In the hot-injection synthesis, metal salt precursors of the form AX and BX<sub>2</sub> are solubilized in a solvent that contains stabilizing ligands, after which the A-site organometallic solution is injected at an elevated temperature into the solution containing BX<sub>2</sub>, and colloidal QDs emerge within seconds.<sup>[1,11,13]</sup>


Perovskite LEDs (PeLEDs) have recently achieved high external quantum efficiencies (EQEs) above 20% in the red and green; but blue PeLEDs have lagged behind their red and green counterparts.<sup>[14,15]</sup> Low

EQEs in blue devices have been attributed to increased degradation pathways through increased defect formation at higher driving voltages; as well as due to lower PLQYs of the initial active layer.<sup>[16–18]</sup> Additionally, PeLED research on deep-blue emission (<470 nm) has been limited. The Rec.2020 standard set by the International Telecommunications Union Radiocommunication (ITU-R) requires blue emitters having emission centered at 467 nm and, by achieving a narrow full-width at half-maximum (FWHM <25 nm) and minimal red tail, to meet the color coordinate: [(x<sub>blue</sub> = 0.131, y<sub>blue</sub> = 0.046)].<sup>[19]</sup>

In order to achieve blue emission in perovskites, halide mixing and quantum confinement strategies are employed. Blue perovskite QDs have relied on anion mixtures containing both Br<sup>-</sup> and Cl<sup>-</sup> within the APbX<sub>3</sub> cubic/orthorhombic nanocrystal, such as in the archetypal CsPbBr<sub>3-x</sub>Cl<sub>x</sub> to obtain the desired emission.<sup>[1,11,20]</sup> These mixed halide systems have enabled high PLQYs and impressively narrow FWHM of 12 nm in solution for pure CsPbCl<sub>3</sub>, and roughly 25 nm for mixed Br/Cl systems.<sup>[10]</sup> Utilizing this strategy, Song et al. achieved an EQE of 0.07% at an emission wavelength of 455 nm and a peak brightness of 742 cd m<sup>-2</sup>.<sup>[20]</sup> A record high EQE of 1.9% was reported by Pan et al. at 490 nm, but these devices displayed low luminance.<sup>[21]</sup> Unfortunately, mixed halide PeLEDs suffer from color instability under operating conditions: phase segregation into pure Cl<sup>-</sup> and Br<sup>-</sup> phases occurs under voltage bias.<sup>[22]</sup> This leads to a red-shift of the electroluminescence (EL) spectra.<sup>[22]</sup>

P. Todorović, Dr. D. Ma, Dr. B. Chen, Dr. R. Quintero-Bermudez, Dr. M. I. Saidaminov, Dr. Y. Dong, Prof. E. H. Sargent  
Department of Electrical and Computer Engineering  
University of Toronto  
10 King's College Road, Toronto, Ontario M5S 3G4, Canada  
E-mail: ted.sargent@utoronto.ca

Prof. Z.-H. Lu  
Department of Materials Science and Engineering  
University of Toronto  
184 College Street, Toronto, Ontario M5S 3E4, Canada

 The ORCID identification number(s) for the author(s) of this article can be found under <https://doi.org/10.1002/adom.201901440>.

DOI: 10.1002/adom.201901440

Nanoplates (NPI) offer an attractive alternative route; however, their higher defect densities have so far led to sub-1% LED EQEs.<sup>[18,23,24]</sup> Recently, Gangishetty et al. demonstrated an EQE of 0.5% at 469 nm and a maximum luminance of 111 cd m<sup>-2</sup> in confined CsPbBr<sub>3-x</sub>Cl<sub>x</sub> nanoplates; but these too exhibited low luminance values at peak EQEs.<sup>[18]</sup> Wu et al. synthesized pure CsPbBr<sub>3</sub> nanoplates with PLQYs approaching unity at emission wavelengths of 463 nm, and achieved a maximum EQE and luminance of 0.12% and 62 cd m<sup>-2</sup>, respectively.<sup>[25]</sup> Recently, Hoyer et al. reported EQEs of 0.55% and 0.3% for sky-blue (489 nm) and blue (464 nm) CsPbBr<sub>3</sub> NPI-based PeLEDs.<sup>[26]</sup> However, further improvements in EQEs and color stability must be achieved for blue PeLEDs to increase further interest.

We hypothesized that a mixed cation approach with a pure bromine phase could provide a route to enlarging the bandgap without incurring voltage-induced phase segregation. We introduce Rb<sup>+</sup> into CsPbBr<sub>3</sub> nanocrystals during synthesis to enlarge the bandgap. Rb-doping in perovskite QDs and quasi-2D thin films have been previously reported, where it was found to blue-shift the absorption and PL properties.<sup>[27-30]</sup>

Here, we report tunable blue emission (450–500 nm) enabled by selecting different nanoscale geometries of Rb<sub>x</sub>Cs<sub>1-x</sub>PbBr<sub>3</sub>, namely nanocubes and nanoplates. We find that the nanocubes exhibit longer wavelengths (>480 nm) and symmetric emission whereas nanoplates display slightly asymmetric profiles but achieve the deepest of blues as a result of stronger quantum confinement. We then explored these materials as active layers, fabricating blue LEDs with EL peaks at 467, 475, and 490 nm, which to date have not been achieved using this material system.

The constituent atoms in the perovskite crystal determine the geometries (Figure 1a) in which they exist under ambient conditions. Equation (1) represents the Goldschmidt tolerance factor (*t*) which describes the stability of perovskites. Stable halide perovskites generally exhibit a *t* value greater than 0.85.

$$t = \frac{r_A + r_X}{\sqrt{2}(r_B + r_X)} \quad (1)$$

We used these metrics to estimate the limit to Rb<sup>+</sup> doping of CsPbBr<sub>3</sub> (*t* = 0.92) with Rb<sup>+</sup> to increase the bandgap. Finite Rb<sup>+</sup> incorporation results in further tilting of the PbX<sub>6</sub> octahedra, reducing the overall orbital overlap and hence opening up the bandgap of CsPbBr<sub>3</sub> while simultaneously reducing the tolerance factor.<sup>[27,28,31-33]</sup> However, it has been reported that an upper bound of 70% Rb<sup>+</sup> exists in a mixed cation perovskite QD, as pure RbPbBr<sub>3</sub> does not exist under ambient conditions.<sup>[34]</sup>

We implemented a hot-injection synthesis, utilizing reactive metallorganic precursors at elevated temperatures. We adapted the procedure of Protescu et al. for CsPbX<sub>3</sub> QDs, modifying the reaction conditions (see the Experimental Section for details) to obtain blue emissive nanocrystals doped with Rb<sup>+</sup>.<sup>[1]</sup> We found that by simultaneously injecting equal volumes of solutions of Cs and Rb-oleate, we obtained nanocrystals of Rb<sub>x</sub>Cs<sub>1-x</sub>PbBr<sub>3</sub> with photoluminescence (PL) peaks in the range of 490 and 502 nm. Then, to further blue-shift the emission, we modulated the reaction temperature and the ratio of OA:OLA to control

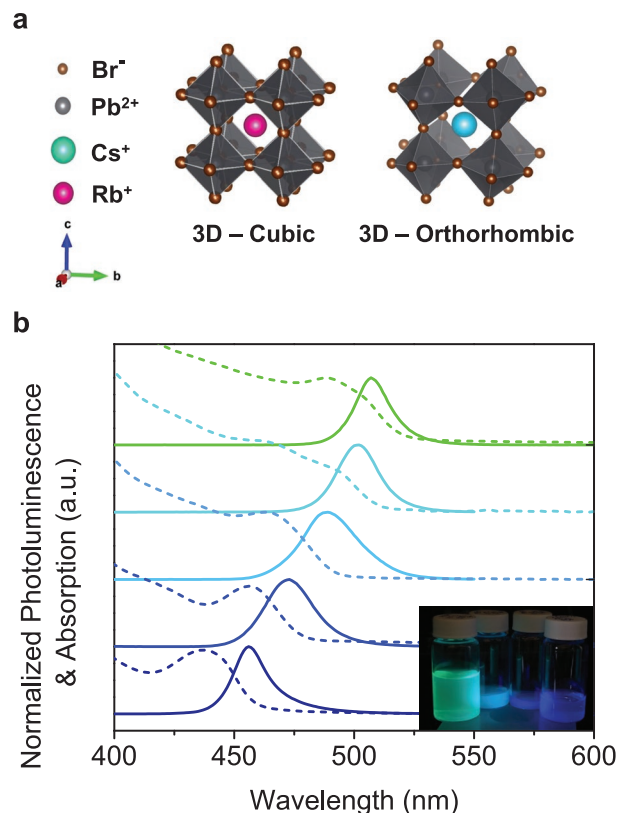


**Figure 1.** a) Perovskite crystal structure, showing both 3D cubic and orthorhombic phases. b) Photoluminescence (solid line) and absorption (dashed line) spectra of the synthesized solutions at various reaction temperatures and conditions. Decreasing temperature from 150 °C leads to smaller particle growth and a blue-shift in the absorption and photoluminescence peak. Control CsPbBr<sub>3</sub> nanocrystals ( $\lambda = 510$  nm) were used as a reference to compare our doping strategy (Table S1, Supporting Information). Inset is a picture of various solutions, illuminated by a UV-LED source ( $\lambda = 374$  nm) displaying the tunable emission.

nanocrystal size. When we maintained the same molar ratio of Rb:Cs (2:1), syntheses carried out at lower reaction temperatures (135 and 120 °C) led to Rb<sub>x</sub>Cs<sub>1-x</sub>PbBr<sub>3</sub> QDs emitting at wavelengths shorter than 480 nm, suggesting slower particle growth and therefore a shift to higher energies as observed in solution PL and absorption peaks (Figure 1b). The PL profiles in Figure 1b are relatively symmetric which is indicative of emission originating from isotropic nanocubes. However, when the volumetric ratio of OA:OLA is changed from 1:1 to 2:1, colloidal nanoplates were observed with deep-blue emission (Figure S1, Supporting Information), peaking in the ranges of 450–470 nm with narrow linewidths (18 nm). The slight asymmetry observed in the PL profiles of these nanoplates arises from the inherent size distribution of varied thickness of nanoplates which occur during synthesis and purification. The absorption was also shifted and sharp exciton peaks for lower reaction temperatures indicate a larger portion of anisotropic quantum confined material. The PLQYs of the Rb<sub>x</sub>Cs<sub>1-x</sub>PbBr<sub>3</sub> solutions ranges from 60% for the deep-blue to 90% for the sky-blue emitting species, which is comparable with CsPbBr<sub>3</sub> QDs (Table S1, Supporting Information).<sup>[1,11]</sup>

Next we investigated the PL lifetime decay of the QDs (Figure S2, Supporting Information). We observed similar radiative lifetimes comparable to those seen of previous reports.<sup>[35]</sup> We summarize these findings in Table S2 in the Supporting Information, where QDs of  $\text{Rb}_x\text{Cs}_{1-x}\text{PbBr}_3$  exhibit slightly shorter radiative lifetimes than  $\text{CsPbBr}_3$  for the same reaction temperature, and enhance further reduction as the temperature is decreased. This is consistent with decreased particle size, and increased trap formation on the surface as a result of the defects which arise at lower reaction temperatures—commonly exhibited in nanoplates which yield lower PLQY values in comparison to their cubic counterparts.<sup>[36]</sup> Introducing  $\text{PbBr}_2$  into a solution of the nanocrystals as a post-treatment method has been seen to improve surface passivation.<sup>[13,36]</sup>

The resulting blue-shift in the optoelectronic properties (PL and absorption spectra) of these quantum dots suggests that the  $\text{Rb}^+$  is incorporated into the  $\text{CsPbBr}_3$  crystals—something not observed under otherwise-identical synthesis conditions without the addition of rubidium oleate. We performed X-ray photoelectron spectroscopy (XPS) measurements on perovskite QD films to further confirm A-site doping. **Figure 2a** indicates the presence of Rb in the films. We note that the XPS spectra of Pb (Figure 2b; Figure S3, Supporting Information) do not change, whereas the Cs peaks shift (Figure 2b) to lower binding energies when Rb is introduced into the perovskite

nanocrystal, which has been previously reported for other A-site doping elements of smaller radii as a result of the change in the electronic density.<sup>[37]</sup> Integration of the results for the given synthesis conditions yields an atomic Cs:Rb ratio 2:1 for nanocubes and 1.5:1 for nanoplates resulting in compositions of the formula  $\text{Rb}_{0.33}\text{Cs}_{0.66}\text{PbBr}_3$  and  $\text{Rb}_{0.4}\text{Cs}_{0.6}\text{PbBr}_3$ , respectively (Table S3, Supporting Information).

Powder X-ray diffraction (XRD) spectra shift to larger  $2\theta$  angles upon  $\text{Rb}^+$  doping (Figure 2d and Figure S4, Supporting Information). The main peaks of pristine  $\text{CsPbBr}_3$  QDs at  $15.08^\circ$  and  $30.42^\circ$  (Figure 2d) correspond to the (100) and (200) crystal planes which increase slightly to  $15.26^\circ$  and  $30.66^\circ$ , respectively upon  $\text{Rb}^+$  doping. This is expected since  $\text{Rb}^+$  is smaller than  $\text{Cs}^+$  effectively: increasing the Pb–Br chemical bond, therefore increasing the tilting of the  $\text{PbBr}_6$  octahedra and shifting the XRD spectra towards larger  $2\theta$  angles which is consistent with  $\text{Cl}^-$  doping of  $\text{CsPbBr}_3$  NCs ( $r_{\text{Cl}^-} > r_{\text{Br}^-}$ ).<sup>[18,38]</sup> The pure  $\text{RbPbBr}_3$  literature values of the XRD peaks (blue) match those of the  $\text{Rb}_x\text{Cs}_{1-x}\text{PbBr}_3$  orthorhombic perovskite QDs, explaining successful incorporation as the peaks are shifting towards the pure Rb-phase. When the temperature and OA/OLA concentration was altered, additional peaks were observed, which we attribute to the  $\text{Rb}_4\text{PbBr}_6$  phase, likely to be synthesized as an energetically favorable by-product (cyan bars in Figure 2d). These measurements give evidence of successful Rb

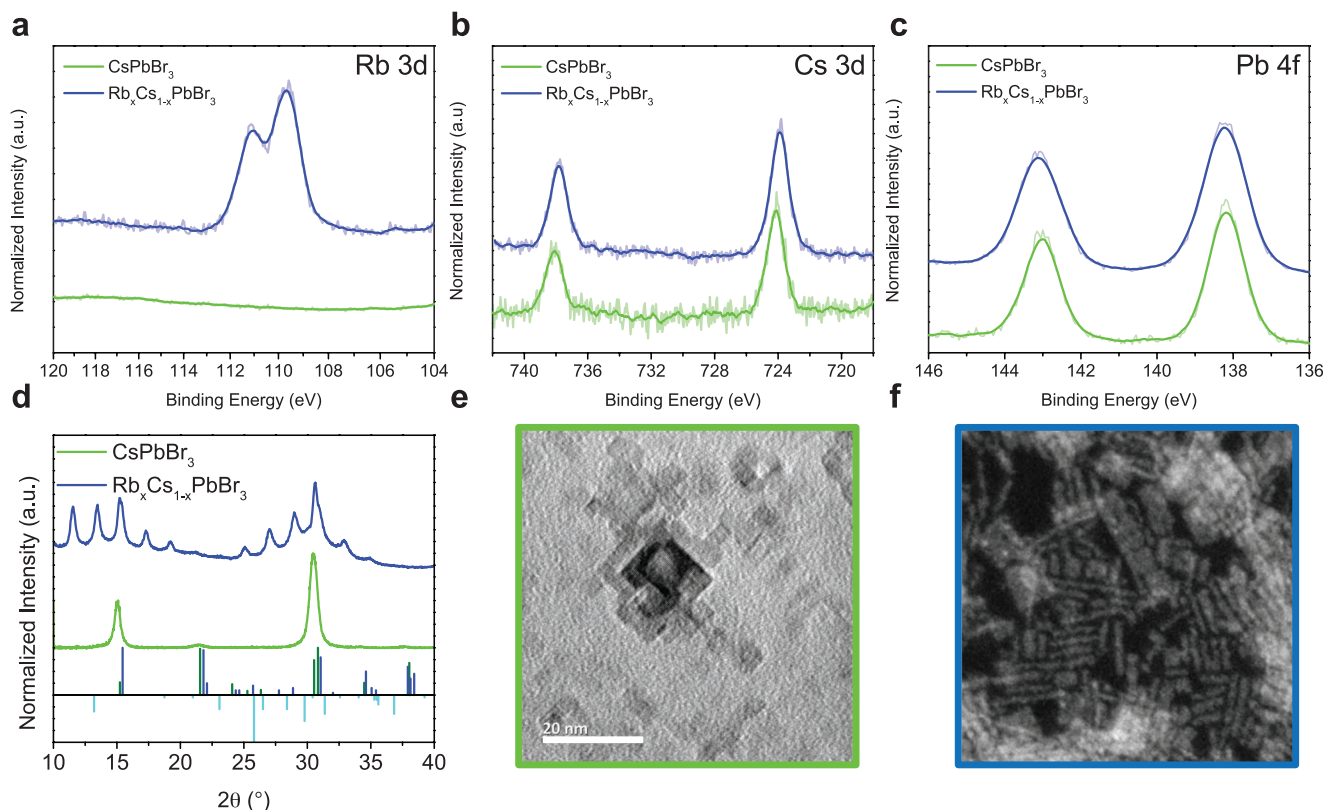


**Figure 2.** Crystal structure characterization. XPS spectra (raw data and 10-point running average smoothing—thick line) of a) Rb, b) Cs, c) Pb of drop-cast PQD films. Rb was present in the synthesized  $\text{Rb}_x\text{Cs}_{1-x}\text{PbBr}_3$  NCs (for all temperatures and reaction conditions). d) XRD spectra of cubic  $\text{CsPbBr}_3$  NCs (green curve) and nanoplates of  $\text{Rb}_x\text{Cs}_{1-x}\text{PbBr}_3$  nanoplates (blue curve). Deep-blue, green and cyan bars underneath the raw spectra correspond to peaks of  $\text{RbPbBr}_3$  (PDF 00-028-0924),  $\text{CsPbBr}_3$  (PDF 00-018-0364), and  $\text{Rb}_4\text{PbBr}_6$  (PDF 00-025-0724) as obtained from the ICDD database. e) TEM images of synthesized  $\text{Rb}_x\text{Cs}_{1-x}\text{PbBr}_3$  nanocubes and f) STEM dark-field image of  $\text{Rb}_x\text{Cs}_{1-x}\text{PbBr}_3$  nanoplates with inset scale bars of 20 nm.

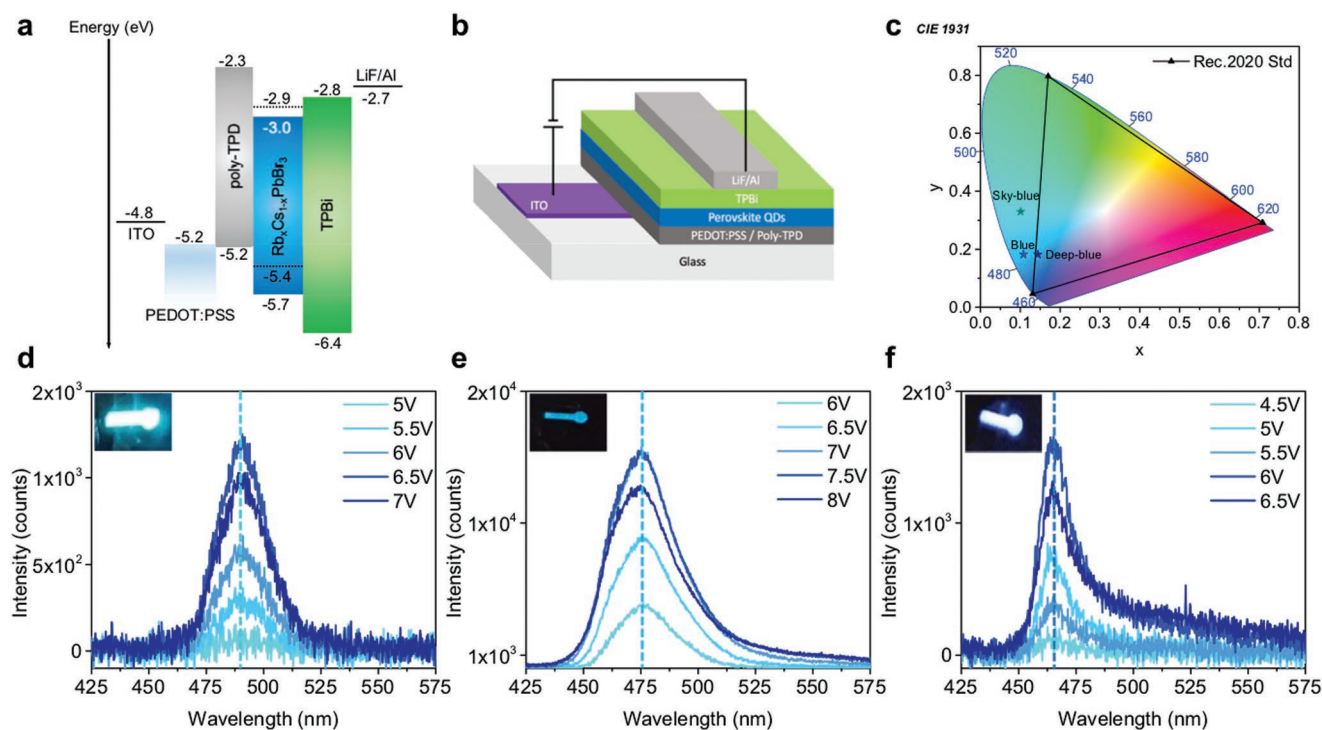


**Figure 3.** PeLEDs fabricated using the  $\text{Rb}_x\text{Cs}_{1-x}\text{PbBr}_3$  NCs. a) Energy level diagram of the PeLEDs, whereby the conduction band and valence band for the active material ( $\text{Rb}_{0.4}\text{Cs}_{0.6}\text{PbBr}_3$  nanoplates and nanocubes, indicated by solid and dashed lines respectively) were obtained by ultraviolet photoelectron spectroscopy (UPS, see Figure S5, Supporting Information). b) Device architecture. c) CIE plot of EL devices and their corresponding location with respect to the Rec. 2020 color standards. Stabilized EL peaks at d) 490 nm, e) 475 nm, and f) 464 nm for sky-blue, blue, and deep-blue emitting devices for various operating voltages. Inset photographs are of EL devices under operating conditions for the various wavelengths.

incorporation into the perovskite QD lattice structure leading to changes of the optoelectronic properties.

We further confirmed the cubic crystal structure through transmission electron microscopy (TEM) images as indicated in Figure 2e, with lateral dimensions of  $\approx 5$  nm. At lower temperatures (120 °C) and at an altered ligand ratio, we obtained small nanoplates and nanoparticles (Figure 2f, Figure S5, Supporting Information), with lateral dimensions of roughly 3–5 nm—consistent with previously synthesized nanoplates of similar composition.<sup>[13,26,36]</sup> Energy dispersive X-ray (EDX) mapping of Rb-doped perovskite QDs corroborate successful Rb<sup>+</sup> incorporation with the presence of Rb on nanoparticles where the signals of Cs, Pb, and Br are present (Figure S6, Supporting Information).

Next we fabricated PeLEDs (architecture in Figure 3a,b): indium tin oxide (ITO)/PEDOT:PSS/poly-TPD/perovskite QDs/TPBi (60 nm)/LiF (1 nm)/Al (150 nm), where PEDOT:PSS is poly(3,4-ethylenedioxythiophene)polystyrene sulfonate, poly-TPD is poly(bis-4-butylphenyl-*N,N*-bisphenyl)benzidine are the hole-transporting layers (HTL) and TPBi is 1,3,5-tris(*N*-phenylbenzi-

miazole-2-yl)benzene is the electron-transporting layer (ETL), respectively. Typically, poly-TPD is implemented as an HTL buffer layer, aiding charge injection and improving the performance of PeLEDs.<sup>[26]</sup> As noted previously, most mixed halide approaches achieve blue emission by introducing Cl<sup>-</sup> (which is known to be a trap and introduce vacancies within the perovskite QDs), but under operating conditions the EL red-shifts considerably.<sup>[36,39,40]</sup> However, the mixed cation approach levers a pure bromine crystal structure, and this results in improved PL and EL stability. We demonstrated stable EL emission across the blue-spectrum from 464 to 490 nm and have provided the Commission Internationale de l'Éclairage (CIE) coordinates for each device in Figure 3c. The EL peaks display no spectral shift when the bias is increased (Figure 3d–f). To our knowledge, these devices are the first reported Rb-doped perovskite QD LEDs that demonstrate high color-purity.<sup>[26]</sup>

The performance results for the sky-blue and deep-blue PeLEDs are tabulated in Table 1 for devices exhibiting the lowest turn-on voltages at a minimal luminance of 10 cd m<sup>-2</sup>. In Figure 4, sky-blue emitting devices exhibited a peak EL

**Table 1.** PeLED electroluminescence performance metrics.

Device	Peak $\lambda_{\text{EL}}$ (FWHM) [nm]	Peak luminance [cd m <sup>-2</sup> ]	Peak EQE <sup>a)</sup> [%]	Luminance (@ EQE <sub>peak</sub> ) [cd m <sup>-2</sup> ]	CIE coordinates (x,y)
Sky-blue	490 (24)	183	0.69	18	(0.101, 0.330)
Deep-blue	464 (18)	63	0.11	29	(0.144, 0.182)

<sup>a)</sup>All EL spectra here recorded had at least a 10 cd m<sup>-2</sup>.

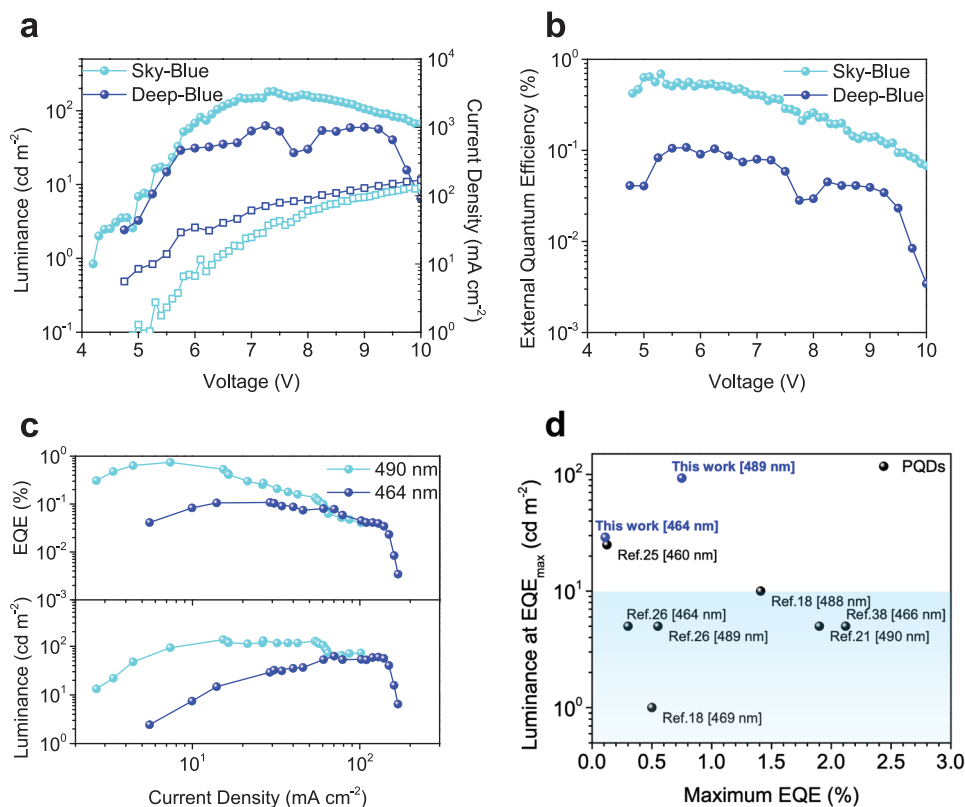


**Figure 4.** PeLEDs fabricated from  $\text{Rb}_x\text{Cs}_{1-x}\text{PbBr}_3$  QDs. a) Current density ( $J$ ) displayed by squares and luminance ( $L$ ) displayed by circles, b) external quantum efficiency (all reported EQE values here are reported with at least  $10 \text{ cd m}^{-2}$  device performances of sky-blue (cyan line) and deep-blue (blue line) as a function of applied bias. c) Devices which exhibited the largest luminance at their peak EQEs (Table 2 summarizes the performance values). d) Comparison of reported perovskite quantum dot device luminance at maximum EQEs [at peak wavelength]. A horizontal line at  $10 \text{ cd m}^{-2}$  segments the data to indicate the importance of luminance at the reported maximum EQEs and highlights the improved device performance of  $\text{Rb}_x\text{Cs}_{1-x}\text{PbBr}_3$  devices.

emission wavelength at 490 nm, a maximum EQE of 0.69% and a maximum luminance of  $183 \text{ cd m}^{-2}$ . The deep-blue devices achieved a maximum EQE of 0.11%, low turn-on voltages of 4 V, narrow and stable EL spectra and maximum luminance of  $63 \text{ cd m}^{-2}$ . The values are comparable to those of previously reported perovskite QDs and nanoplates, but an order of magnitude higher in the observed luminance at peak EQE metric (Figure 4d, Table S4, Supporting Information). The best performing  $\text{Rb}_x\text{Cs}_{1-x}\text{PbBr}_3$  PeLEDs are summarized in **Table 2**, with a maximum EQE of 0.87% (Figure S8, Supporting Information) and peak luminance at the maximum EQE of  $93 \text{ cd m}^{-2}$  at 0.75% (Figure 4c) for the sky-blue emitting devices (histogram of devices reported in Figure S9, Supporting Information). We attribute the low EQE values in the deep-blue devices as a result of the decreasing PLQY of the materials as further washing steps are introduced. The increased washing

cycles reduce the surface passivation, inducing a larger portion of defects and nonradiative recombination pathways. In addition to perovskite QD surface passivation strategies, reducing interfacial losses in the device architecture may further advance the device performance.<sup>[25,26,38,41–43]</sup>

In this work, we successfully synthesized stable blue-emitting perovskite QDs via the incorporation of  $\text{Rb}^+$  in the A-site of  $\text{CsPbBr}_3$  nanocrystals. These materials displayed high PLQYs (>60%) and tunable yet stable photoluminescence. We fabricated the first blue-emitting Rb-doped PeLEDs to span the wavelength range from deep-blue (464 nm) to sky-blue (490 nm) and report EQEs of 0.11% to 0.87%, respectively. The  $\text{Rb}_x\text{Cs}_{1-x}\text{PbBr}_3$  QDs exhibit some of the narrowest emission linewidths (18 nm) and good EL operating stabilities at high applied bias conditions. These A-site doped QDs offer thermal stability and operational stability, since halide segregation is avoided.

**Table 2.** Best  $\text{Rb}_x\text{Cs}_{1-x}\text{PbBr}_3$  PeLED performance.

Device	Peak $\lambda_{\text{EL}}$ (FWHM) [nm]	Peak luminance [ $\text{cd m}^{-2}$ ]	Peak EQE [%]	Luminance (@ EQE <sub>peak</sub> ) [ $\text{cd m}^{-2}$ ]
Sky-blue	490 (22)	186	0.87	93 @ 0.75%
Deep-blue	464 (18)	71	0.11	29 @ 0.11%

## Experimental Section

**Materials:** All chemicals used are commercially available and were used as received without any additional purification steps: lead (II) bromide ( $\text{PbBr}_2$ , Alfa-Aesar Puratronic, 99.998%), cesium carbonate ( $\text{Cs}_2\text{CO}_3$ , Sigma-Aldrich, 99%), rubidium carbonate ( $\text{Rb}_2\text{CO}_3$ ,

Sigma-Aldrich, 99%), oleic acid (OA, Sigma-Aldrich, 98%), oleylamine (OLA, Caledon), octadecene (ODE, Caledon), ethyl acetate (EtAc, anhydrous, Sigma-Aldrich, 99.8%), methyl acetate (MeAc, anhydrous, Sigma-Aldrich, 99.8%), hexane (anhydrous, Alfa-Aesar), octane (Alfa-Aesar), and chlorobenzene (anhydrous, Sigma-Aldrich). PEDOT:PSS (Clevios PVP Al 4083) was purchased from Heraeus. Poly-TPD was purchased from American Dye Source. 1,3,5-tris(*N*-phenylbenzimidazole-2-yl)benzene (TPBi) was purchased from Lumtec.

**Synthesis of Rb-Oleate:**  $\text{Rb}_2\text{CO}_3$  (0.430 g, 1.86 mmol, Sigma-Aldrich 99%) was added to ODE (20 mL) and OA (1.5 mL) in a 100 mL round-bottom flask. The mixture was heated to 120 °C under vacuum and dried for 1 h. Then, the flask was put under nitrogen and heated to 150 °C for complete dissolution and formation of Rb-oleate.

**Synthesis of Cs-Oleate:**  $\text{Cs}_2\text{CO}_3$  (0.433 g, 1.33 mmol, Sigma-Aldrich 99%) was added to ODE (20 mL) and OA (1.25 mL) in a 100 mL round-bottom flask. The mixture was heated to 120 °C under vacuum and dried for 1 h. Then, the flask was put under nitrogen and heated to 150 °C for complete dissolution and formation of Cs-oleate.

**Synthesis of  $\text{Rb}_x\text{Cs}_{1-x}\text{PbBr}_3$  Nanocrystals:**  $\text{PbBr}_2$  (0.068 g, 0.187 mmol, Alfa-Aesar, 99.99%) was dissolved in ODE (5 mL) along with oleic acid and oleyl amine (1:1 volumetric ratio, 1 mL each). The solution was degassed for a total of 1 h at 120 °C, then switched over to a pure nitrogen environment and heated to 150 °C to fully dissolve any remaining  $\text{PbBr}_2$ . Upon heating, a 0.4 mL mixture of Rb-oleate (0.23 mL)/(0.17 mL) Cs-oleate solution was injected into this  $\text{PbBr}_2$  solution at various temperatures (120–150 °C). Nanoplates were synthesized by modifying the ratio of OA:OLA from 1:1 to 2:1, yielding anisotropic growth. After 15 s of injection, the crude solution was cooled in an ice-water bath. In addition, the nanocrystals can be synthesized in a one-step precursor injection by simultaneously dissolving both  $\text{Cs}_2\text{CO}_3$  (0.215 g) and  $\text{Rb}_2\text{CO}_3$  (0.215 g) in ODE (20 mL) and OA (1.5 mL) in a 100 mL reaction flask and heated to same reaction conditions as for the individual oleate precursors. Then 0.4 mL of this mixed oleate solution was injected into the Pb-oleate solution.

**Purification of  $\text{Rb}_x\text{Cs}_{1-x}\text{PbBr}_3$  Nanocrystals:** Upon cooling down to room temperature, the crude solution was collected, and centrifuged at 7830 rpm for 10 min. The resulting supernatant was discarded, and the precipitate containing the perovskite quantum dots was collected by redispersion in hexane (2 mL). A mixture of methyl acetate and ethyl acetate (1:1 volumetric, 6 mL total) was added to precipitate the solubilized nanocrystals. The resulting mixture was then centrifuged once again at 7830 rpm for 5 min. The supernatant was discarded and the precipitate was redispersed into hexane or octane for further measurements.

**Photoluminescence (PL) and Absorption Measurements:** Photoluminescence measurements were done using a Horiba Fluorolog time-correlated single photon counting system equipped with UV/vis/NIR photomultiplier tube detectors, dual grating spectrometers, and a monochromatized xenon lamp excitation source. A pulsed UV laser diode ( $\lambda = 374$  nm) was used to acquire the transient PL signal. Absolute PLQY values were measured by coupling a Quantum-Phi integrating sphere to the Fluorolog system through optical fibres. All PLQY measurements followed published methods.<sup>[44]</sup> Optical absorption measurements were carried out in a Lambda 950 UV–vis–IR spectrophotometer.

**XRD Measurements:** XRD measurements were conducted using a Rigaku MiniFlex 600 diffractometer (Bragg-Brentano geometry) equipped with a NaI scintillation counter detector and a monochromatized  $\text{Cu K}\alpha$  radiation source ( $\lambda = 1.5406$  Å) operating at a voltage of 40 kV and current of 15 mA.

**XPS Measurement:** XPS measurements were carried out with the Thermo Scientific K-Alpha XPS system. An Al  $\text{K}\alpha$  source with a 400  $\mu\text{m}$  spot size was used for measurements to detect photo-electrons at specific energy ranges to determine the presence of specific elements.

**Electron Microscopy:** Bright field and high angle annular dark field (HAADF) images were collected at an acceleration voltage of 300 kV using a Hitachi HF-3300 electron microscope. Elemental mapping was acquired by a Bruker EDX spectroscopic detector.

**UPS Measurement:** UPS spectra were measured on ITO substrates with high conductivity. Photoelectron spectroscopy was performed in a PHI5500 Multi-Technique system using non-monochromatized He- $1\alpha$  radiation ( $h\nu = 21.22$  eV). All the work function and valence band measurements were performed at a take-off angle of 88°, with the base chamber pressure of  $10^{-7}$  Pa. A bias of  $-5$  V was applied to measure the work function.

**LED Fabrication:** First 100  $\Omega$   $\text{sq}^{-1}$  ITO-coated glass substrates were sequentially cleaned by detergent, deionized water, acetone, and isopropanol in an ultrasonic washer, then treated by ultraviolet ozone plasma for 5 min and employed as the anode. Then a solution of PEDOT:PSS was spin coated at 500 rpm for 10 s then 4500 rpm for 90 s, followed by annealing on a hot plate at 150 °C for 20 min in the air ambient. The substrates were cooled down and transferred into a nitrogen-filled glovebox. Poly-TPD (3.5  $\text{mg mL}^{-1}$  in chlorobenzene) was spin coated at 2000 rpm for 60 s (1000  $\text{rpm s}^{-1}$  ramp) and annealed at 100 °C for 10 min in a nitrogen-filled glovebox, leading to a thickness of roughly 10 nm. On top of this layer, perovskite QDs dispersed in octane (10  $\text{mg mL}^{-1}$ ) were spin coated at 2000 rpm for 60 s (1000  $\text{rpm s}^{-1}$  ramp). Finally, the substrates were transferred into a high vacuum thermal evaporator, where TPBi (60 nm), LiF (1 nm) and Al (150 nm) were deposited thereon layer by layer through a shadow mask under a high vacuum of less than  $10^{-4}$  Pa. The device active area was 6.14  $\text{mm}^2$  as defined by the overlapping area of the ITO and Al electrodes. The devices were encapsulated before the measurements, using an ultraviolet curable resin (exposure under ultraviolet light for 20 s) and covered on the edges between the device and a transparent glass chip.

**LED Evaluation:** All devices were tested under ambient condition. The luminance versus voltages and the current density versus voltage characteristics were collected using a HP4140B picoammeter. The absolute EL power spectra were collected using an integrating sphere and an Ocean Optics USB4000 spectrometer by mounting of the devices on the wall of the integrating sphere. The EQEs were then calculated through the measured absolute EL power spectra and the current density.

## Supporting Information

Supporting Information is available from the Wiley Online Library or from the author.

## Acknowledgements

P.T. and D.M. contributed equally to this work. P.T. wrote the manuscript and led all experimental work. D.M. helped to fabricate light-emitting diodes. B.C. helped with electron microscopy characterization of materials. P.T. would like to thank Sjoerd Hoogland for his valuable insights and discussions. E.H.S supervised this work and provided edits to the manuscript. The authors would like to acknowledge Dr. Jimi Tjong, Paul Dellock, and Harry Lobo from Ford Motor Company for their valuable discussions. This work was financially supported by Natural Sciences and Engineering Research Council of Canada (NSERC). This work was also partially funded by Ford PDC, Ford PERDC, and Ford's University Research Program (URP). P.T. acknowledges funding from NSERC. M.I.S. acknowledges the support of Banting Postdoctoral Fellowship Program.

## Conflict of Interest

The authors declare no conflict of interest.

## Keywords

blue emission, halide perovskites, LEDs, light-emitting diodes, perovskite quantum dots

Received: August 22, 2019  
Published online:

- [1] L. Protesescu, S. Yakunin, M. I. Bodnarchuk, F. Krieg, R. Caputo, C. H. Hendon, R. X. Yang, A. Walsh, M. V. Kovalenko, *Nano Lett.* **2015**, *15*, 3692.
- [2] M. M. Lee, J. Teuscher, T. Miyasaka, T. N. Murakami, H. J. Snaith, *Science* **2012**, *338*, 643.
- [3] Z. K. Tan, R. S. Moghaddam, M. L. Lai, P. Docampo, R. Higler, F. Deschler, M. Price, A. Sadhanala, L. M. Pazos, D. Credgington, F. Hanusch, T. Bein, H. J. Snaith, R. H. Friend, *Nat. Nanotechnol.* **2014**, *9*, 687.
- [4] W. S. Yang, J. H. Noh, N. J. Jeon, Y. C. Kim, S. Ryu, J. Seo, S. Il Seok, *Science* **2015**, *348*, 1234.
- [5] Y. Ling, Z. Yuan, Y. Tian, X. Wang, J. C. Wang, Y. Xin, K. Hanson, B. Ma, H. Gao, *Adv. Mater.* **2016**, *28*, 305.
- [6] L. Zhang, X. Yang, Q. Jiang, P. Wang, Z. Yin, X. Zhang, H. Tan, Y. M. Yang, M. Wei, B. R. Sutherland, E. H. Sargent, J. You, *Nat. Commun.* **2017**, *8*, 15640.
- [7] S. D. Stranks, H. J. Snaith, *Nat. Nanotechnol.* **2015**, *10*, 391.
- [8] M. Grätzel, *Nat. Mater.* **2014**, *13*, 838.
- [9] S. D. Stranks, G. E. Eperon, G. Grancini, C. Menelaou, M. J. P. Alcocer, T. Leijtens, L. M. Herz, A. Petrozza, H. J. Snaith, *Science* **2013**, *342*, 341.
- [10] G. Nedelcu, L. Protesescu, S. Yakunin, M. I. Bodnarchuk, M. J. Grotevent, M. V. Kovalenko, *Nano Lett.* **2015**, *15*, 5635.
- [11] Q. A. Akkerman, V. D'Innocenzo, S. Accornero, A. Scarpellini, A. Petrozza, M. Prato, L. Manna, *J. Am. Chem. Soc.* **2015**, *137*, 10276.
- [12] Y. Wang, X. Li, J. Song, L. Xiao, H. Zeng, H. Sun, *Adv. Mater.* **2015**, *27*, 7101.
- [13] Q. A. Akkerman, G. Rainò, M. V. Kovalenko, L. Manna, *Nat. Mater.* **2018**, *17*, 394.
- [14] T. Chiba, Y. Hayashi, H. Ebe, K. Hoshi, J. Sato, S. Sato, Y. J. Pu, S. Ohisa, J. Kido, *Nat. Photonics* **2018**, *12*, 681.
- [15] K. Lin, J. Xing, L. N. Quan, F. P. G. de Arquer, X. Gong, J. Lu, L. Xie, W. Zhao, D. Zhang, C. Yan, W. Li, X. Liu, Y. Lu, J. Kirman, E. H. Sargent, Q. Xiong, Z. Wei, *Nature* **2018**, *562*, 245.
- [16] Z. Li, Z. Chen, Y. Yang, Q. Xue, H. L. Yip, Y. Cao, *Nat. Commun.* **2019**, *10*, 1027.
- [17] N. K. Kumawat, X. K. Liu, D. Kabra, F. Gao, *Nanoscale* **2019**, *11*, 2109.
- [18] M. K. Gangishetty, S. Hou, Q. Quan, D. N. Congreve, *Adv. Mater.* **2018**, *30*, 1706626.
- [19] International Telecommunication Union, *Recomm. ITU-R BT.2020-2* **2015**.
- [20] J. Song, J. Li, X. Li, L. Xu, Y. Dong, H. Zeng, *Adv. Mater.* **2015**, *27*, 7162.
- [21] J. Pan, L. N. Quan, Y. Zhao, W. Peng, B. Murali, S. P. Sarmah, M. Yuan, L. Sinatra, N. M. Alyami, J. Liu, E. Yassitepe, Z. Yang, O. Voznyy, R. Comin, M. N. Hedhili, O. F. Mohammed, Z. H. Lu, D. H. Kim, E. H. Sargent, O. M. Bakr, *Adv. Mater.* **2016**, *28*, 8718.
- [22] G. Li, F. W. R. Rivarola, N. J. L. K. Davis, S. Bai, T. C. Jellicoe, F. De La Peña, S. Hou, C. Ducati, F. Gao, R. H. Friend, N. C. Greenham, Z. K. Tan, *Adv. Mater.* **2016**, *28*, 3528.
- [23] D. N. Congreve, M. C. Weidman, M. Seitz, W. Paritmongkol, N. S. Dahod, W. A. Tisdale, *ACS Photonics* **2017**, *4*, 476.
- [24] D. Yang, Y. Zou, P. Li, Q. Liu, L. Wu, H. Hu, Y. Xu, B. Sun, Q. Zhang, S. T. Lee, *Nano Energy* **2018**, *47*, 235.
- [25] Y. Wu, C. Wei, X. Li, Y. Li, S. Qiu, W. Shen, B. Cai, Z. Sun, D. Yang, Z. Deng, H. Zeng, *ACS Energy Lett.* **2018**, *3*, 2030.
- [26] R. L. Z. Hoyer, M. L. Lai, M. Anaya, Y. Tong, K. Gałkowski, T. Doherty, W. Li, T. N. Huq, S. Mackowski, L. Polavarapu, J. Feldmann, J. L. Macmanus-Driscoll, R. H. Friend, A. S. Urban, S. D. Stranks, *ACS Energy Lett.* **2019**, *4*, 1181.
- [27] H. Wu, Y. Yang, D. Zhou, K. Li, J. Yu, J. Han, Z. Li, Z. Long, J. Ma, J. Qiu, *Nanoscale* **2018**, *10*, 3429.
- [28] D. Amgar, T. Binyamin, V. Uvarov, L. Etgar, *Nanoscale* **2018**, *10*, 6060.
- [29] S. Baek, S. Kim, J. Y. Noh, J. H. Heo, S. H. Im, K.-H. Hong, S.-W. Kim, *Adv. Opt. Mater.* **2018**, *15*, 1800295.
- [30] Y. H. Park, I. Jeong, S. Bae, H. J. Son, P. Lee, J. Lee, C. H. Lee, M. J. Ko, *Adv. Funct. Mater.* **2017**, *27*, 1605988.
- [31] Y. Jiang, C. Qin, M. Cui, T. He, K. Liu, Y. Huang, M. Luo, L. Zhang, H. Xu, S. Li, J. Wei, Z. Liu, H. Wang, G. H. Kim, M. Yuan, J. Chen, *Nat. Commun.* **2019**, *10*, 1868.
- [32] M. R. Linaburg, E. T. McClure, J. D. Majher, P. M. Woodward, *Chem. Mater.* **2017**, *29*, 3507.
- [33] A. E. Maughan, A. M. Ganose, M. A. Almaker, D. O. Scanlon, J. R. Neilson, *Chem. Mater.* **2018**, *30*, 3909.
- [34] J. W. Xiao, Y. Liang, S. Zhang, Y. Zhao, Y. Li, Q. Chen, *Chem. - Eur. J.* **2019**, *25*, 2597.
- [35] L. Protesescu, S. Yakunin, S. Kumar, J. Bär, F. Bertolotti, N. Masciocchi, A. Guagliardi, M. Grotevent, I. Shorubalko, M. I. Bodnarchuk, C. J. Shih, M. V. Kovalenko, *ACS Nano* **2017**, *11*, 3119.
- [36] B. J. Bohn, Y. Tong, M. Gramlich, M. L. Lai, M. Döblinger, K. Wang, R. L. Z. Hoyer, P. Müller-Buschbaum, S. D. Stranks, A. S. Urban, L. Polavarapu, J. Feldmann, *Nano Lett.* **2018**, *18*, 5231.
- [37] Y. Liu, G. Pan, R. Wang, H. Shao, H. Wang, W. Xu, H. Cui, H. Song, *Nanoscale* **2018**, *10*, 14067.
- [38] S. Hou, M. K. Gangishetty, Q. Quan, D. N. Congreve, *Joule* **2018**, *2*, 2421.
- [39] A. Walsh, S. D. Stranks, *ACS Energy Lett.* **2018**, *3*, 1983.
- [40] Y. Wu, X. Li, H. Zeng, *ACS Energy Lett.* **2019**, *4*, 673.
- [41] Y. Zhou, J. Chen, O. M. Bakr, H. T. Sun, *Chem. Mater.* **2018**, *30*, 6589.
- [42] Y. Zou, Z. Yuan, S. Bai, F. Gao, B. Sun, *Mater. Today Nano* **2019**, *5*, 100028.
- [43] J. Shamsi, A. S. Urban, M. Imran, L. De Trizio, L. Manna, *Chem. Rev.* **2019**, *119*, 3296.
- [44] J. C. de Mello, H. F. Wittmann, R. H. Friend, *Adv. Mater.* **1997**, *9*, 230.